Mechanical properties of multi-stable morphing skin structures with large deformation capability

Ke Huang[*], Jiaying Zhang[†]

Beihang University, Beijing 100191, China

Chen Wang[‡]

Nanjing University of Aeronautics and Astronautics, Jiangsu 210016, China

Qingyun Wang[§]

Beihang University, Beijing 100191, China

Alexander D. Shaw[¶], Michael I. Friswell[**]

Swansea University, Swansea SA1 8EN, United Kingdom

Abstract. This paper presents a multi-stable morphing skin structure (MMSS) to achieve low in-plane stiffness, high out-of-plane stiffness, and high strain capacity. It is based on bi-stable pre-shaped curved beams (BPCBs), which enable large deformations through stable state transitions rather than linear elastic deformation. The in-plane mechanical properties are analyzed using large deformation beam theory and potential energy landscape approaches. The mechanical response of the theorical model is in good agreement with both numerical and experimental results. The out-of-plane mechanical property is studied using standard three-point bending tests, which shows that the hybrid array form, can significantly enhance out-of-plane stiffness. The MMSS offers advantages in reducing actuation energy consumption and overcoming parasitic resistance in flexible structures.

Keywords. Morphing skin, Multi-stable metamaterial, Morphing aircraft, Stable switching, Standard three-point bending test

[*] PhD Candidate, Department of Aerospace Engineering.
[†] Associate Professor, School of Aeronautic Science and Engineering; jiaying.zhang@buaa.edu.cn (Corresponding Author).
[‡] Professor, College of Aerospace Engineering.
[§] Professor, School of Aeronautic Science and Engineering.
[¶] Senior Lecturer, Department of Aerospace Engineering.
[**] Emeritus Professor, Department of Aerospace Engineering.

Nomenclature

Abbreviations

MM	=	mechanical metamaterial
MMM	=	multi-stable mechanical metamaterial
MMSS	=	multi-stable metamaterial skin structure
BPCB	=	bi-stable pre-shaped curved beam
FEM	=	finite element methods
MSBM	=	multi-stable basic module
LM	=	linear elasticity materials
SM	=	superelastic materials

1. Introduction

Morphing aircraft can actively adapt their aerodynamic shapes according to flight conditions to ensure optimal aerodynamic efficiency [1-4]. However, to achieve additional degrees of freedom in deformation based on the fixed geometric shape of traditional aircraft, further research is needed around morphing structures, distributed high-energy density actuators, flight control strategies, and morphing skins [1,5].

Morphing aircraft usually require morphing skins distinct from traditional rigid skins to ensure the continuity of the lifting surfaces. Morphing skins should have sufficient stiffness to withstand aerodynamic loads while maintaining enough flexibility to reduce the actuators' demand [6]. Therefore, a composite skin structure concept based on lattice metamaterial cores and flexible surface layers has been proposed to meet such conflicting design requirements [7]. Mechanical metamaterials (MM) are artificially designed composite materials with programmable and outstanding properties influenced by the micro-architectures and spatial arrangements of unit cells [8]. In contrast to traditional materials designed based on constitutive relationships, MM design allows for a wide array of possibilities for elasticity tensors of anisotropic materials with up to 21 independent coefficients to give a vast design region. It is possible to construct any form of elasticity tensor by designing micro architectures consisting of isotropic materials and vacuum without violating thermodynamics [9]. This offers the opportunity to tailor mechanical properties by designing the geometric structure of these periodic unit cells to achieve the desired mechanical characteristics, amplifying small deformations within each unit through periodic arrays [10,11]. Currently, MMs can achieve

novel properties such as complex multi-stability, tunable stiffness, and negative Poisson's ratio [8,12].

Traditional honeycomb structures have periodic cell shapes, including hexagonal [7,13], accordion-shaped [14], corrugated plates [15], chiral [16], and star-shaped [17,18]. Huang and Leng [19] proposed a novel negative Poisson's ratio honeycomb and analysed its in-plane mechanical performance. Chen and Shen [20] investigated the in-plane mechanical characteristics of zero Poisson's ratio honeycombs, taking into account geometric and material nonlinearities in two-dimensional deformations. Jha and Dayyani [21] optimized the deformation performance of fish-like zero Poisson's ratio units, demonstrating the potential use of these units in lattice metamaterials as support structures for morphing wing skins.

In contrast to traditional honeycomb structures, multi-stable mechanical metamaterial (MMM) refers to MM that have two or more stable states in static equilibrium, with energy barriers between each stable state. Transitioning between states requires absorbing energy to overcome these barriers and then releasing energy [22,23]. Therefore, lattice metamaterials have significant advantages in reducing actuation energy consumption due to multiple stable states during loading as they are designed with multi-stable modules that combine the anisotropic stiffness characteristics [24,25]. Currently, MMMs fall into several categories: (1) designs based on flexible shells and beams [26-28]; (2) asymmetric laminated structures based on differences in fibre and matrix thermal expansion coefficients [29-31]; (3) origami-based MMMs [32-35]; (4) magnetically driven MMMs [36].

MMs have widespread applications in shape reconfiguration, mechanical logic operations, and reusable energy absorption. Restrepo et al.[37] proposed a phase transforming cellular material and experimentally studied its hysteresis and sawtooth-like loading characteristics. This cellular material maintains the structural recoverability while achieving the same energy absorption performance as traditional cellular materials. Restrepo et al.[38] introduced morphological imperfections into shape-memory polymer-based periodic cellular structures, enabling the controlled adjustment of effective mechanical properties after fabrication. Shi et al.[39] designed a shell structure with strategically distributed holes, creating a programmable multi-stable perforated shell that allows for one-, two-, or three-directional multi-stability. The programmable energy damping performance of this structure was validated through low-speed impact hammer tests and RC car collision tests. Chen et al.[40] designed a programmable bistable MM array that allows for the repeated programming and stable storage of complex mechanical properties. Mei et al.[41] developed a programmable MM based on buckling

bistable beams, capable of performing basic logical operations, and demonstrated its ability to store information in a small-size design. Boston et al.[42-43] proposed the concept of a meta-beam based on a multi-stable honeycomb structure, which serves as a competitive candidate for the wing spars of morphing wings, achieving low in-plane deformation energy consumption and high out-of-plane stiffness.

For arrays of interacting bistable units, more complex out-of-plane deformations or changes in mechanical properties can occur. Udani and Arrieta[44-45] studied the mechanisms of geometric instability in arrays of bistable shell elements and introduced the concept of "taming" geometric instabilities, enabling access to any globally unstable state. The presence of such geometric instabilities allows switching between a plate-like response with no stretching-bending coupling and a shell-like response with both in-plane and out-of-plane deformation coupling. Faber et al. [46] applied hierarchical multi-stable behavior in these MMMs to soft robotic grippers, mechanical memory, and logic computation scenarios. Liu et al. [27] revealed the deformation mechanisms of bistable elements in flexible sheets, noting that their bistable characteristics depend on the ratio between size and Pogorelov scale. A single element exhibits azimuthal instability, while multi-element arrays can maintain symmetric buckling under specific strain conditions.

Due to the vast design space of metamaterials and the various stable state transition and negative stiffness characteristics of MMMs [9,26], combined with the energy balance concept [47,48], MMMs have great potential in reducing actuation requirements and improving energy efficiency when integrated with compliant mechanisms. Integrating these advantages into actuating morphing wings through morphing skin structures enhances the performance of such compliant mechanisms.

This paper proposes a multi-stable metamaterial skin structure (MMSS) that is based on bi-stable pre-shaped curved beam (BPCB) units and supporting structures. Harnessing elastic instabilities enables large, reconfigurable shape changes, allowing the structure to achieve high stiffness while maintaining relatively low actuation requirements[42]. In contrast to elastomers deformed by axial tension or traditional honeycomb structures that amplify small bending deformations through periodic arrays, both require energy input for deformation and to maintain the deformed state. However, a MMSS only needs to overcome the potential energy barrier between stable states, enabling it to snap and naturally stabilize in the desired configuration.

The research focuses on the in-plane deformation and out-of-plane bending stiffness, using the theory of large deformation beams and the potential energy landscapes approach. Nonlinear finite element methods (FEM) and experimental analysis are used to study the in-plane mechanical characteristics and out-of-plane bending stiffness under large deformation conditions. The analysis investigates the influence of unit cell geometric parameters, support structure types, and unit cell array configurations on mechanical properties.

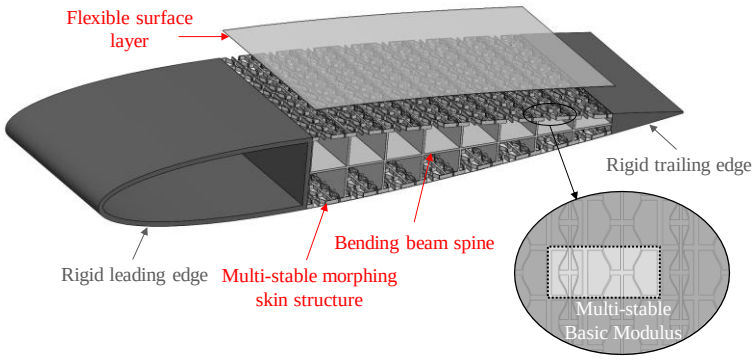

Figure 1. Schematic of the proposed multi-stable morphing skin.

2. Multi-stable morphing skin structures

2.1. Design scheme

The multi-stable morphing skin proposed in this paper consists of a MMSS and a flexible surface layer, as shown in Fig. 1. The multi-stable basic module (MSBM) of the MMSS, highlighted within the circular frame, is composed of four BPCB units. It can be seen that some BPCBs in a stress-free state are compressed into another stable state, which allows stable state transitions under both tension and compressive loads. Therefore, this structure can achieve the desired tension and compressive properties in a one-dimensional direction. As shown in Figure 1, when the camber morphing wing undergoes a downward curvature change, the upper and lower surfaces experience tensile and compressive deformations along the chord direction, respectively. Similarly, this structure can be applied to morphing skins for spanwise and chordwise morphing wings[1].

Figure 2 illustrates the two basic units of the MMM studied in this paper: the diamond-shaped unit and the hexagonal unit, shown in Figs. 2(a) and 2(b) respectively. In the figures, the red lines represent the BPCBs, while the black lines denote the supporting structures. Both types of cells can be viewed as variants of traditional hexagonal honeycomb units.

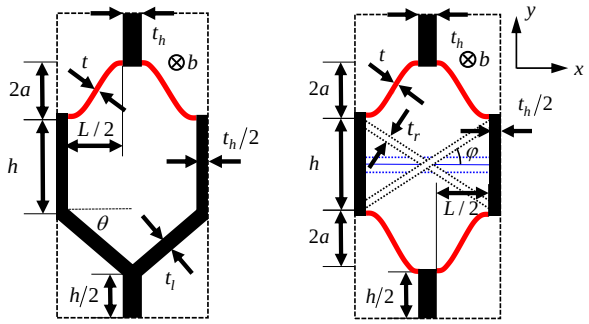

Figure 2. Schematic representation of unit cells showing the geometric parameters of the a) diamond-shaped unit and (b) hexagonal unit

The expression for the displacement of the bi-stable curved beam is given by the cosine function

$$w_0(x) = a\left[1 - \cos\left(\frac{2\pi x}{L}\right)\right] \qquad x \in (0, L) \tag{1}$$

where t, b and L represent the thickness, width and length of the curved beam and a is the amplitude of the cosine function, which is half the height of the curved beam. t_h and h represent the thickness and length of the vertical rods, t_l and l represent the thickness and length of the inclined beams, and θ is the inclination angle of the inclined beams. It is noteworthy that when θ is 0°, the inclined beams transform into horizontal beams, changing the supporting structure from a "Y" shape to a "U" shape. Stiffening ribs were added to the hexagonal basic units to avoid weaker boundary rigidity, which can influence the bi-stable properties of the units, as shown in Fig. 2(b). t_r represents the rib thickness, and φ represents the rib inclination angle. The black and blue dashed lines in the figure represent the maximum and minimum positions of the rib inclination angle within geometric constraints. When the rib inclination angle is at its minimum value of 0°, the fork-shaped ribs merge into a horizontal rib with a thickness of $2t_r$, changing the supporting structure from an "X" shape to an "H" shape.

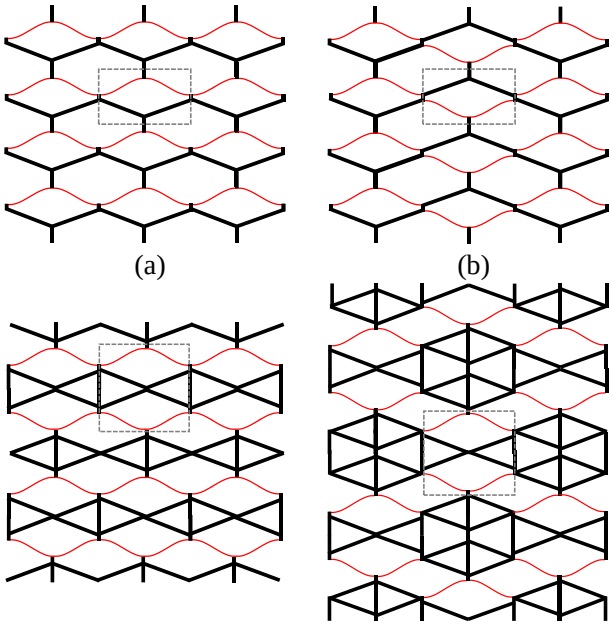

Figure 3. Unit array forms: (a) linear array of diamond-shaped units (b) hybrid array of diamond-shaped unit (c) linear array of hexagonal units (d) hybrid array of hexagonal units

The basic units can be arranged in two array forms: linear array and hybrid array, as shown in Fig. 3. Fig. 3(a) and 3(b) display the two array configurations for the diamond-shaped units, while Fig. 3(c) and 3(d) illustrate the array configurations for the hexagonal units. To ensure internal continuity of the structure, additional supporting structures were added to the hexagonal unit arrays. This modification helps maintain the connectivity of the MMSSs.

2.2. Bi-stable Mechanism of BPCB Units

In reference [49], the BPCB units were thoroughly studied based on the mode superposition method and the principle of minimum potential energy. In this paper, all the BPCB units can be regarded as pre-shaped curved beam models, loaded at the center and fixed at both ends. When the structural parameter $Q = 2a/t \leq 2.31$, the normalized force-displacement relation of the unit may be expressed as [49]

$$F_1 = \frac{3\pi^4 Q^2}{2}\Delta\left(\Delta - \frac{3}{2} + \sqrt{\frac{1}{4} - \frac{4}{3Q^2}}\right)\left(\Delta - \frac{3}{2} - \sqrt{\frac{1}{4} - \frac{4}{3Q^2}}\right) \tag{2}$$

where F_1 and Δ are the normalized generalized force of the first mode and central displacement, and

$$F_i = \frac{8 f_i L^3}{EIh}, \qquad \Delta = \frac{d}{2a} \tag{3}$$

where E is the elastic modulus of the material, I is the moment of inertia of the cross-section, f_i is the generalized force of the i th mode, and d is the actual central displacement.

As Q increases, the second or third buckling modes will be triggered. Neglecting higher-order modes, the load-displacement curve can be described by the combination of generalized force-displacement curves of the second-order mode F_2 or the third-order mode F_3 and F_1. The expressions for F_2 and F_3 are given by [49]

$$F_2 = 4.18\pi^4 - 2.18\pi^4\Delta \tag{4}$$

$$F_3 = 8\pi^4 - 6\pi^4\Delta \tag{5}$$

As shown in Fig. 4, both F_2 and F_3 are negative-slope straight lines and are independent of the structural parameter Q. The constraint of the support structure limits the second-order mode, ensuring the existence of F_3. F_1 is related to the structural parameter Q and is constant when Δ= 0,1,2. When Q=1.67, F_1 and F_2 are tangent; when Q = 2.31, F_1 and F_3 are tangent. It can be observed that F_3 has a region where the force is less than zero, indicating the presence of two stable states, hence the bi-stable phenomenon. To ensure the bi-stable characteristics of the pre-shaped curved beam, Q must be greater than 2.31.

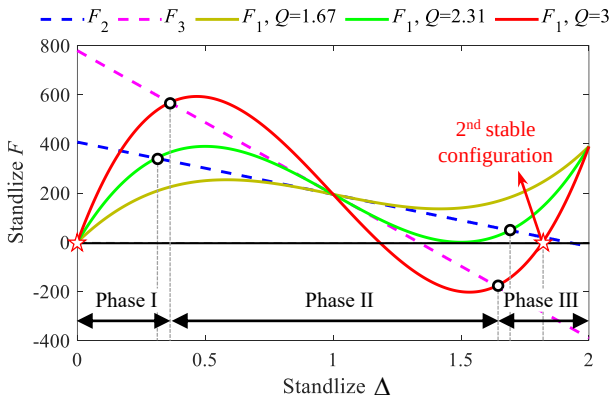

Figure 4. Curved beam force–displacement relation.

2.3. Influence of structural parameters on the mechanical properties of BPCB Units

To utilize BPCB units in the application of morphing skins, it is essential to fully understand their force-displacement characteristics and the maximum stress during the stable state

transition. This section analyses the influence of different structure parameters on the mechanical properties of the BPCB units.

Figure 5 shows force-displacement curves of the BPCBs. (d_{top}, f_{top}), (d_{bot}, f_{bot}), (d_{mid},0) and (d_{end},0) is the top point, the bottom point, the unstable equilibrium point and the second stable equilibrium point on the curve, respectively. Limit force point represents the maximum or minimum force in the mechanical response of a bistable structure. Critical point represents the emergence or disappearance of higher-order modes in the force-displacement characteristic. For a curved beam with bi-stable characteristics, when a load is applied from the pre-shaped stress-free state point (0,0), the structure exhibits positive nonlinear stiffness in the first phase. After reaching the first critical point that triggers higher-order modes, the structural configuration changes, and the structure shows negative stiffness characteristics in the second phase. After passing the saddle point of the structure, a reverse force is generated. Once the structure response returns to the first-order mode, the structure loses its negative stiffness characteristics in the second critical point, showing positive nonlinear stiffness characteristics in the third phase until it reaches the second stable configuration. In the second phase, the negative stiffness region is not entirely linear. When $Q > 2.78$, the negative stiffness segment is linear. When $2.31 < Q < 2.78$, the negative stiffness segment is not completely linear, and the critical point and the limit force point do not coincide.

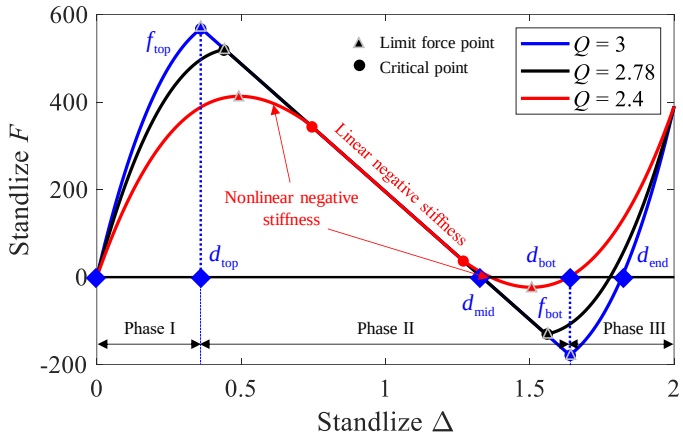

Figure 5. Force-displacement relations of BPCBs.

The relationships between the force of the top point f_{top} and the ratios of structural parameter t/L and $2a/L$ for BPCBs are shown in Fig. 6(a). Figure 6(b) illustrates the relationships between f_{bot} and these two parameter ratios. L was fixed at 30 mm, and E was set to 2.14 MPa. In Fig. 6(b), the white region indicates the absence of the snap-through phenomenon, indicating no occurrence of negative stiffness regions in the force-displacement characteristics. The region

between the lower right bound of the white region and the red solid line indicates the presence of the snap-through phenomenon but no second stable state. The red solid line represents Q = 2.31. In the lower right region of the red solid line, a second stable state exists, meaning that BPCB units can choose parameters from this area. From the force-displacement characteristics, it can be seen that with the increase of t/L and $2a/L$, f_{top} increases.

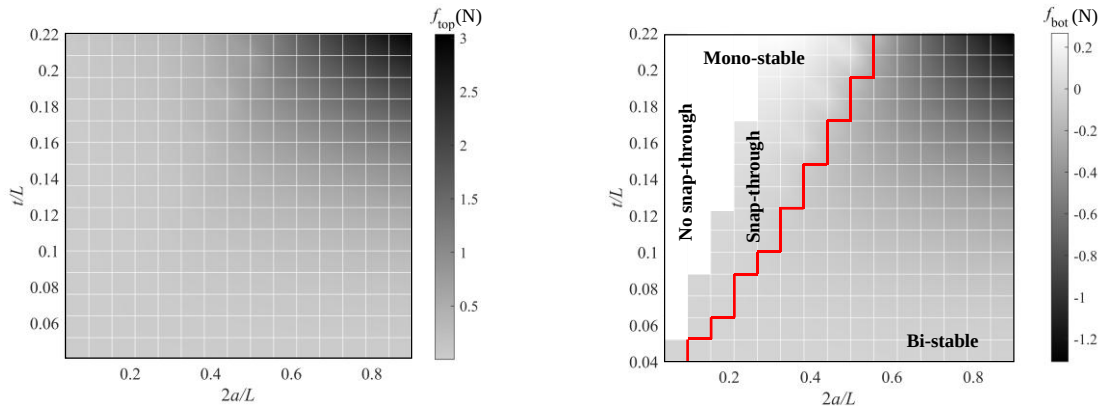

(a) (b)

Figure 6. Relationships between limit force and the two parameter ratios.

However, f_{bot} is the critical parameter to determine the bistable property and the relationship between t/L and $2a/L$ with f_{bot} is relatively more complex. In the mono-stable and snap-through phenomenon region, f_{bot} increases with the increase of t/L and decreases with the increase of $2a/L$. In the bi-stable region, the f_{bot} exhibits a similar trend with increasing $2a/L$, while its relationship with t/L is non-monotonic, initially decreasing and then increasing as t/L increases.

To ensure that the morphing skin avoids structural failure, it is crucial to determine the maximum stress state of the MMSS. During the state-switching process, the structure primarily subjected to strain is the BPCB units. The stress state of the BPCB includes bending stress and axial stress. In references [50], it is known that when $Q \in [2.31,2.36]$, the expression for the maximum stress σ_{max} is

$$\sigma_{max} = \pi^2 \frac{2Eta}{L^2}\left(1 + \frac{1}{Q} + \frac{Q}{4}\right) \tag{6}$$

For Q > 2.36, the expression for the maximum stress σ_{max} is

$$\sigma_{max} = \pi^2 \frac{2Eta}{L^2}\left(1 + \frac{4}{3Q} + \sqrt{5}\sqrt{1 - \frac{16}{3Q^2}}\right) \tag{7}$$

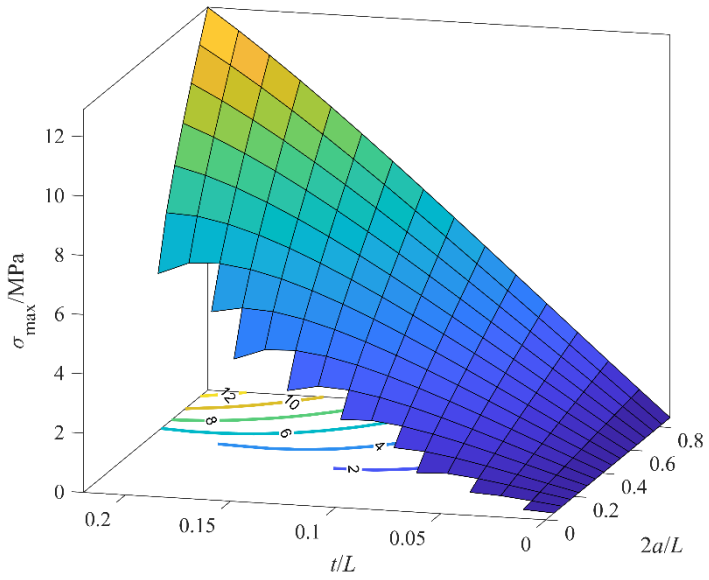

Figure 7. Surface diagram of σ_{max} with respect to two parameter ratios.

The relationships between the σ_{max}, the ratios of the structural parameters t/L and $2a/L$ for BPCBs are showed in Fig. 7. When the parameter t/L is constant, σ_{max} monotonically increases with the parameter $2a/L$. When the parameter $2a/L$ is constant, the analysis based on Eqs. (6) and (7) shows that as t/L increases, σ_{max} first increases and then decreases, reaching its maximum at Q = 2.62. After determining the structure parameters, an important requirement for BPCBs is to ensure that σ_{max} remains below the critical limit σ_{crit}. The σ_{crit} needs to be determined based on material parameters such as the yield strength, fatigue limit, and fracture limit. Therefore, the range of feasible structural parameters can be determined once the σ_{crit} is specified. Clearly, for materials like metals, hard polymers, and ceramics, which have relatively small yield strains, the feasible parameter range is smaller. In contrast, elastomeric materials, which can withstand larger strains and return to their original state, offer a larger parameter range.

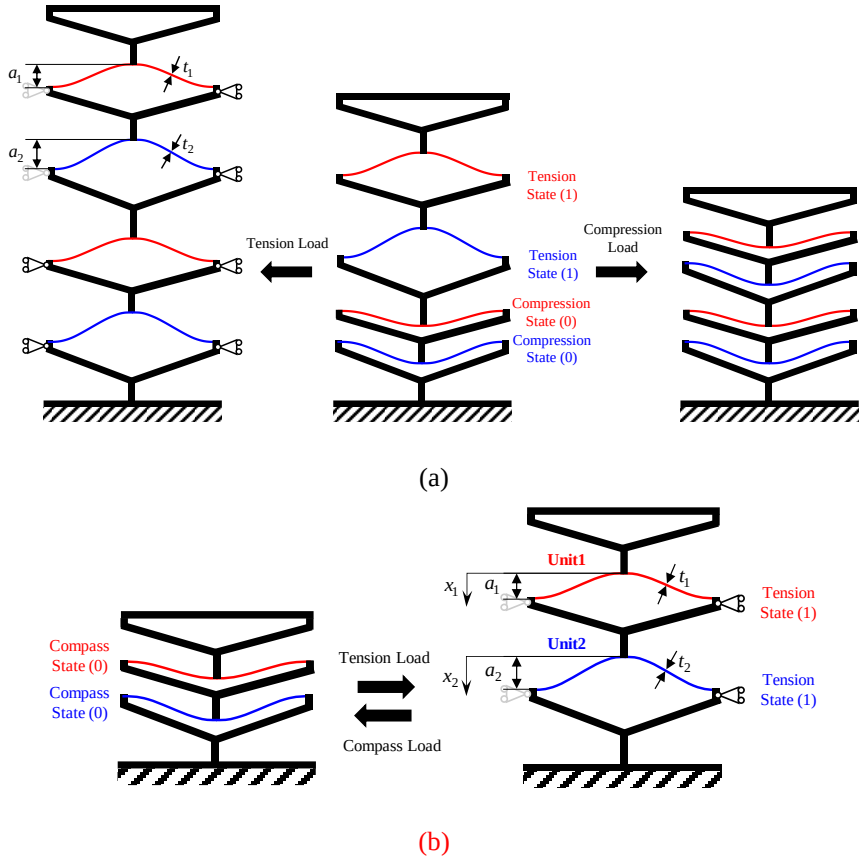

Figure 8. MMSS and simplified model: (a) MSBM of the MMSS (b) Simplified two-unit series structure.

3. In-plane mechanical properties

3.1. Multistable mechanical properties of the MMSS

The original MSBM concept is shown in Fig. 8(a). This module is formed by connecting four BPCB units in series, with two groups of BPCB units having the same geometric parameters (red and blue). After preloading, one unit of each pair is in a compressed state, while the other is in a tension state. Therefore, once compressive load is added, the displacement response of the unit in the compressed state is minimal and can be ignored. The significant deformation is mainly achieved by the state switching of the units in the tension state (without preload units), and vice versa when subjected to tensile load. As a result, the initial multi-stable basic module can be simplified to having only two BPCB units with mechanical response, as shown in Fig. 8(b). In other words, when the original MSBM is stretched, the two units in the compressed state switch to the tension state, and when compressed, the two units in the tension state switch to the compressed state.

This paper takes a_1 = 12 mm, a_2 = 8 mm, b = 10 mm, $t_1 = t_2$ = 2 mm, L = 60 mm for the BPCBs, and the material elastic modulus E = 25.56 MPa as parameters to construct the two-unit series structure. In order to obtain the force-displacement characteristics during the stable state transition of a series structure, the potential energy-displacement curve can be derived by integrating the force-displacement curve of the BPCB unit. The expression for potential energy is

$$E_i(d) = \int_0^d F_i(\delta)d\delta \tag{8}$$

where δ represents the relative displacement of each BPCB unit.

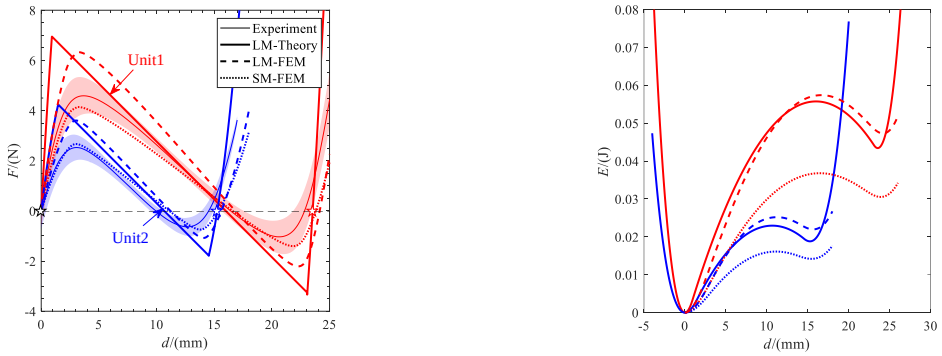

(a) (b)

Figure 9. Statics and potential energy characteristics of curved beams: (a) Force-displacement curve (b) Potential energy-displacement curve.

Based on Eqs. (2) to (5) and (8), the force-displacement curve and the potential energy curve of a single unit are shown in Figs. 9(a) and 9(b). These figures include theoretical solutions, finite element analysis results based on the assumptions of linear elasticity materials (LM) and superelastic materials (SM), and the results of uniaxial loading experiments. Subsequent potential energy calculations are based on the theoretical solutions, and the simulation and experimental setups are discussed later in this paper. By summing the potential energy of the two units, the total potential energy contour map can be obtained. Establishing the coordinate system as shown in Fig. 8(b), the end displacement of unit 1 is denoted as x_1, and the center displacement of unit 2 is denoted as x_2.

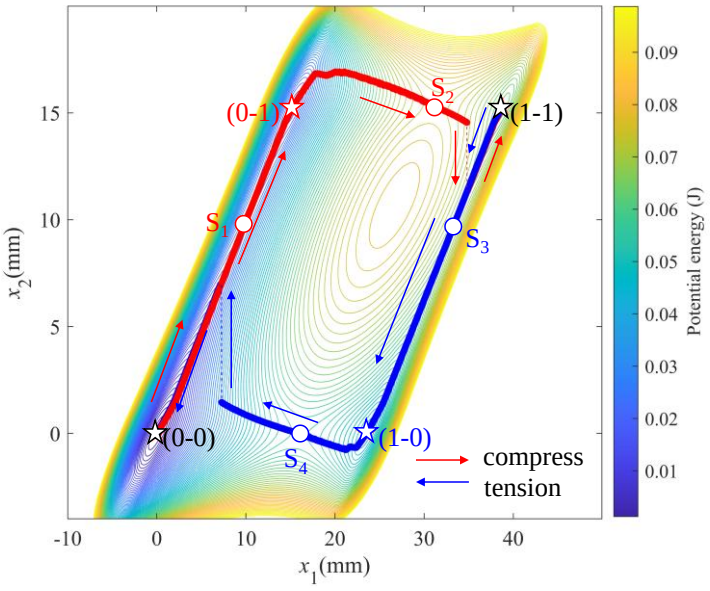

(a)

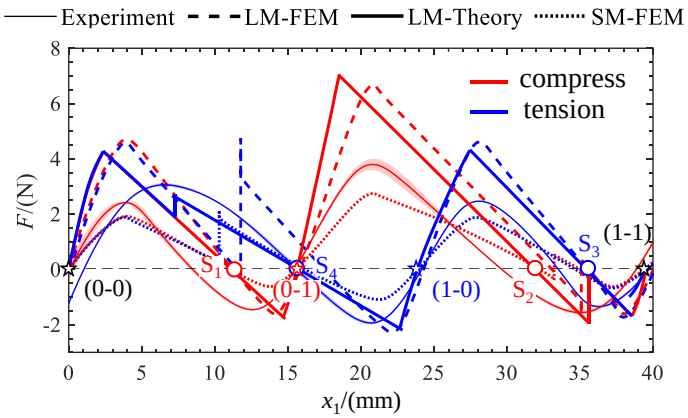

(b)

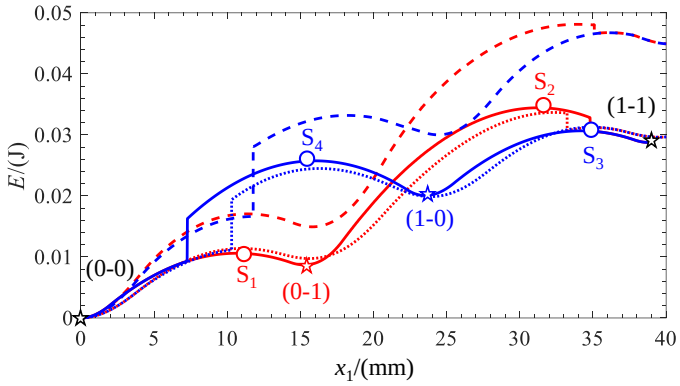

(c)

Figure 10. Mechanical response of the two-unit series structure: (a) Potential energy contour-plot and evolution trajectory (b) Force-displacement curve (c) Potential energy curve.

Based on the unit parameters, the total potential energy E_{tot} of the two-unit series structure is calculated, the expression for the total potential energy is

$$E_{\mathrm{tot}}(x_1, x_2) = \int_0^{x_1 - x_2} F_1(\delta)d\delta + \int_0^{x_2} F_2(\delta)d\delta \tag{9}$$

As shown in Fig. 10(a), the potential energy hypersurface has four potential wells (pentagram marks in Fig. 10(a)), indicating that the structure has four stable configurations. By considering the tension and compressive loading processes as displacement loads, the local potential energy minima corresponding to each load step can be calculated, and the potential energy evolution trajectories of the quasi-static tension and compressive processes of the two-unit series structure can be found on the potential energy map, as shown in Fig. 10(a) and 10(c). Furthermore, the force-displacement curve of the two-unit series structure is obtained, as shown in Fig. 10(b).

Through analysis, it can be found that the structure does not traverse all four stable states during the quasi-static loading process, which is consistent with the conclusions in reference [51]. During the compressive process, the configuration evolves from (0-0) to (0-1), then jumps to the (1-1) configuration after crossing the saddle point S2, without passing through the (1-0) configuration. Conversely, during the tension process, the configuration evolves from (1-1) to (1-0), and after one jump after crossing the saddle point S4, it returns to the (0-0) configuration.

Therefore, based on the theory in reference [49,50], adjusting the geometric parameters of the BPCB units can affect their mechanical response [52], allowing for further customization of mechanical properties. For example, the stable equilibrium point can be designed in the desired long-term usage configuration, and the position of the unstable equilibrium point can be designed to provide a desired negative stiffness. Therefore, such negative stiffness can be balanced to positive stiffness at this point for realizing low-energy-consumptions actuation [31,47,48].

3.2. Standard Tensile Test

Thermoplastic polyurethane (TPU) was selected to prepare the experimental specimens. The elastic modulus and SM properties of the material were measured through uniaxial tensile tests. The uniaxial tensile specimens were designed according to ASTM D412. Three test specimens were tested using a universal testing machine, SUNS UTM4503. The loading speed was set at 5 mm/min, and a large deformation extensometer was used to measure the displacement of the

gauge section during the uniaxial tensile process. Figures 11(a) and 11(b) show the experimental setup and the test results. Due to the large strain produced by the TPU uniaxial tensile specimens, the true stress-strain curve was calculated by collecting the nominal stress-strain curve. By performing linear fitting on the portion where the strain is less than 0.05, the elastic modulus used in theoretical calculations was obtained, resulting in a value of 25.56 MPa.

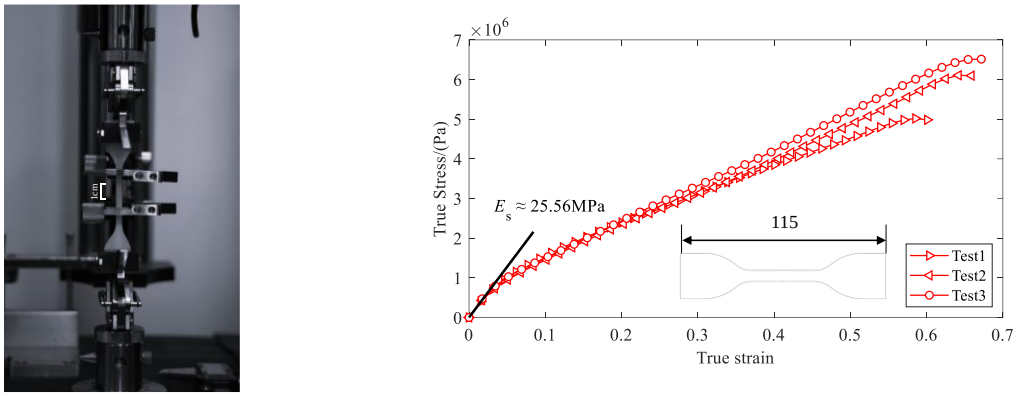

(a) (b)

Figure 11. Experimental characterisation : (a) Experimental setup (b) Test results.

3.3. FEM and Experimental Verification

Abaqus/Standard was employed to investigate the mechanical characteristics during the loading process of PBCBs and their corresponding simplified two-unit series structure. A 3D model was established in Catia and imported into Abaqus for analysis. All subsequent related works were conducted using the same software. Given the nonlinear behavior of TPU under large deformations, simulations were conducted under both LM and SM assumptions to assess their respective influences on the results.

The material elastic model was based on data obtained from standard tensile tests, and its superelastic behavior was fitted using the Yeoh model [53]. Solid models based on LM and SM were meshed using C3D8R and C3D8RH elements, respectively. The thickness direction of the beam was discretized with 6 elements, and 150 elements were used in the longitudinal direction to ensure accuracy and efficiency. Geometric nonlinearity was considered in the loading steps, and self-contact was enabled in simulations to avoid potential contact issues. All simulations were conducted under the "Static, General" analysis type. The models and boundary conditions used in the analysis are shown in Fig. 12.

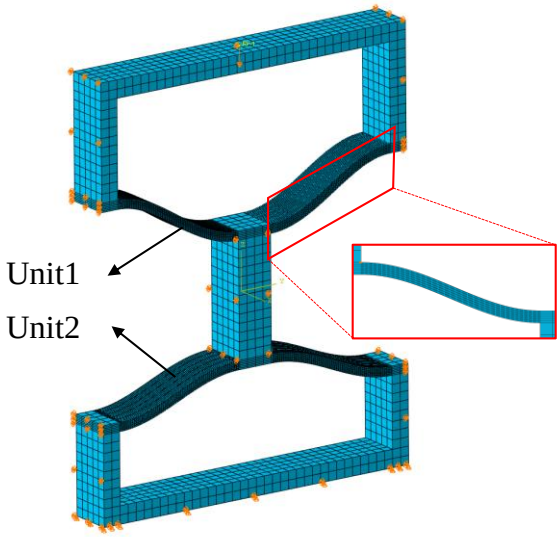

Figure 12. Finite element model.

The results of different stable configurations obtained from FEM simulations are shown in Fig. 13. The evolution of stable configurations obtained from FEM simulations aligns with those calculated using the potential energy landscapes approach, validating the simplification of the MSBM proposed in this paper with two-unit series structure. In the preloaded MSBM, the upper two BPCBs are in the (0-0) state, while the lower two are in the (1-1) state. When the structure is subjected to tension loads, mainly the lower preloaded part is involved, corresponding to the tension process shown in Fig. 13(a). Conversely, when the structure is subjected to compressive loads, mainly the upper part is involved, corresponding to the compression process shown in Fig. 13(a).

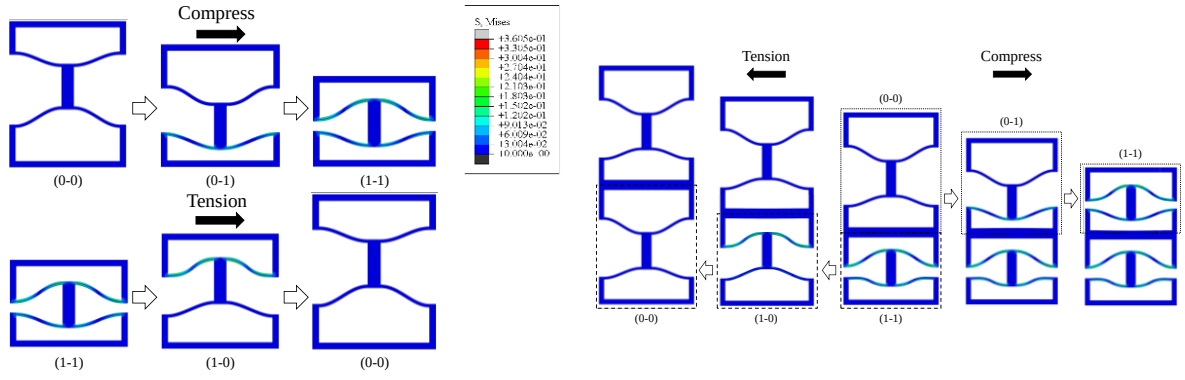

Figure 13. Different stable configurations: (a) Simplified two-unit series structure (b) MSBM.

The specimens were processed using selective laser sintering (SLS), and the materials and processing techniques used were consistent with the standard tensile tests. The prepared specimens underwent uniaxial compression-tension cyclic tests using a universal testing machine. To enhance measurement accuracy, three sets of experimental data were collected and averaged with standard deviations calculated. Figure 14 shows photographs of the experimental tests. To ensure boundary condition stiffness, polymethyl methacrylate (PMMA) with a higher elastic modulus was adhered to the outer sides of the processed test specimens. Details regarding PMMA material properties and processing methods are provided in the subsequent sections.

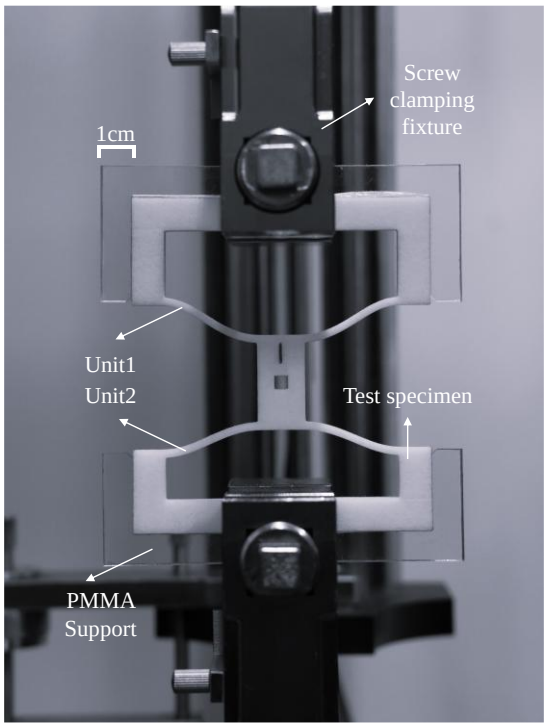

Figure 14. Simplified two-unit series structure test.

The numerical and experimental results of the force-displacement curves and potential energy-displacement curves for the PBCB unit and the two-unit series structure are shown in Fig. 9 and Fig. 10. In Fig. 9, the thin solid line and the shaded area represent the mean value and the standard deviation of the experiments. The thick solid line, dashed line, and dotted line represent the results of the LM theoretical model, the LM FEM model, and the SM FEM model, respectively. In Fig. 10, the dashed line represents the experimental results, and the thick solid line, dotted line, and circle-dashed line represent the results of the LM theoretical model, the LM FEM model, and the SM FEM model, respectively.

Comparing the results reveals that the theoretical model shows a certain accuracy in predicting the force-displacement response, stable configuration, and equilibrium states of the BPSBs. The potential energy landscape approach has certain accuracy in predicting mechanical properties, stable configurations, and potential energy evolution trend of the MMSS. Regarding constitutive theory, it is observed that neglecting superelasticity when modeling large deformation in flexible materials leads to some deviation. The theoretical solution aligns well with the LM FEM, while the experimental results are in better agreement with the SM FEM. The linear elastic Young's modulus of the SM, which considers only small strain experimental results, tends to overestimate the material modulus, resulting in higher mechanical responses in the LM model compared to the SM model.

To enable rapid design of the MSBM, the theoretical model offers significant computational efficiency while maintaining a satisfactory prediction accuracy even neglecting superelasticity. The buckling mode superposition theory of Euler beams presents considerable errors in handling large preformed bending angles and thick beams requiring shear deformation consideration. High-order nonlinear beam theory, considering shear deformation, can be employed to improve computational accuracy [50,52].

Table 1. Structural dimensions and simulation parameters in the model.

Parameter	*Value*	*Parameter*	*Value*
Elasticity modulus E /GPa	1.86	t_l /mm	4
Poisson ratio v	0.4	t_r /mm	2
a /mm	3	h (Diamond-shaped unit) /mm	6
t /mm	1.25	h (Hexagonal unit) /mm	12
L /mm	30	φ / °	[0,30]
t_h /mm	4	θ / °	[0,30]

4. Out-of-plane mechanical properties

4.1. FEM modeling

To support a flexible surface with low in-plane stiffness and high strain capability in the deformation direction, a multi-stable array metamaterial skin structure also needs sufficient rigidity to support out-of-plane aerodynamic loads. The structure under bending loads shifts from global bending to local twisting deformation by utilizing BPCBs. Therefore, finite

element modeling is employed to analyze the impact of the support structure type and key structural parameters on the bending stiffness of the proposed multi-stable skin structure. Standard three-point bending tests are carried out following ASTM D790 to analyze the out-of-plane bending stiffness of the structure.

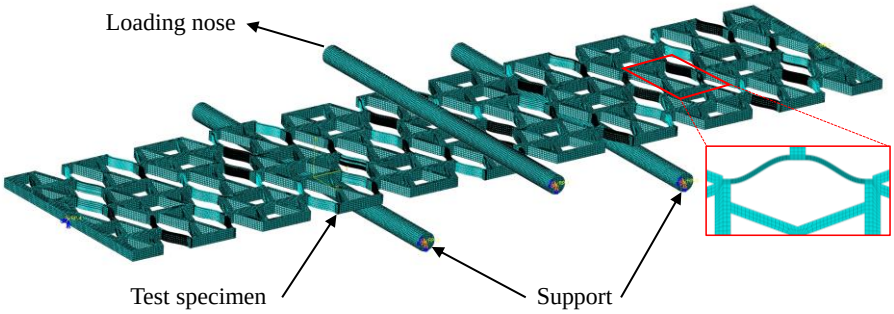

Figure 15. Multistable basic module test.

According to ASTM D790 standards, the experiments and FEM use a 10mm diameter rod for both the loading head and support, with a span of 160mm and thickness of 5mm. All modules were arranged in a 10×3 array using units of the same size, as shown in Fig. 2 for the basic unit and Fig. 3 for the array configuration. Simulation parameters for this section are detailed in Table 1, allowing calculation of the module width as 114mm. The simulation meshing and type settings were consistent with Section 3.3, with the loading head modeled as a rigid body. By applying a downward displacement load of 10mm to the loading head and recording the resulting reaction force, the equivalent bending stiffness of the structure was calculated. The FEM model is shown in Fig. 15.

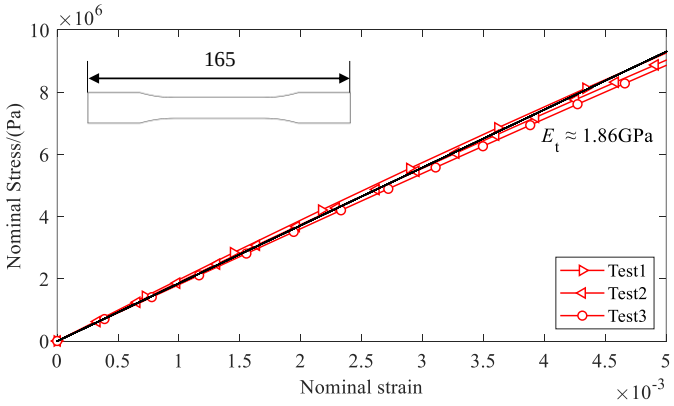

Figure 16. Material test results.

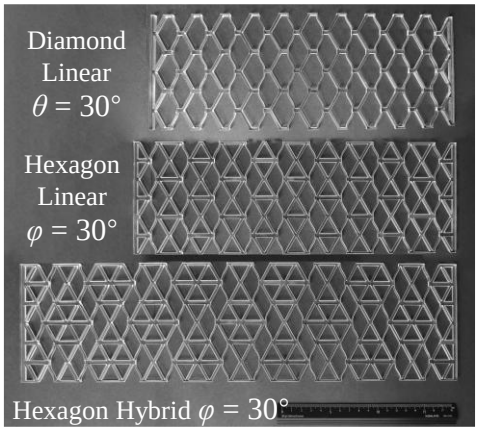

(a)

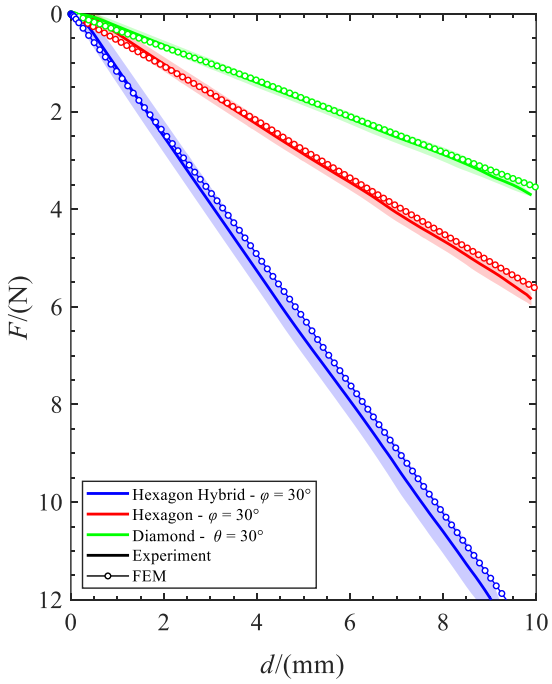

(b)

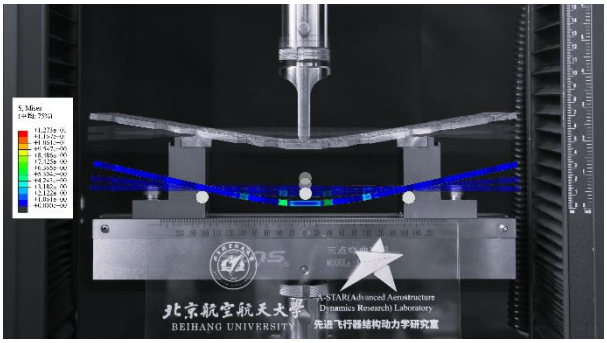

(c)

Figure 17. Results of the standard three-point bending test: (a) Test specimen (b) Force-deflection curve (c) Deformation correlation.

4.2. Experimental verification

Transparent PMMA sheets were selected and processed into test specimens using CO_2 laser cutting. Parametric models for different basic units and array configurations were created using Catia, and the test specimens were fabricated using laser cutting. Following ASTM D882 standards for processing material test specimens, mechanical properties were firstly tested. Nominal displacement during uniaxial tensile testing was measured using an extensometer. Fig. 16 shows the results of the material testing, and linear interpolation of the results yielded a Young's modulus of 1.86 GPa.

The three-point bending experiment was conducted using a universal testing machine at a loading speed of 2 mm/s, with three cycles of loading to 15 mm, averaging the results and calculating the standard deviation. FEM models were adjusted based on the dimensions of the actual machined three-point bending specimens, as shown in Fig. 17(a). Comparison of the force-displacement relationship and deformation results obtained from simulations and experiments, is illustrated in Fig. 17(b) and 17(c). The specimen in Fig. 17(c) features a hexagonal unit linear array. It is evident that the FEM results closely match the experimental results in mechanical response and deformation, demonstrating that the computational accuracy of the FEM model is sufficient to study the influence of support structure types and key structural parameters on the bending stiffness of the MMSS.

4.3. The influences of support structure types and array configurations

Figure 18(a) shows the force-deflection curves for unit cells, array forms, and different inclination angles, compared with traditional hexagonal honeycombs. The traditional hexagonal honeycomb selected for comparison has the same dimensions as the diamond-shaped MMM. The BPCBs of the MMM are replaced with inclined beams, as shown in the inset within the black frame in the figure. According to ASTM D790 standard, the expression for the equivalent bending stiffness E_{B} of the structure is given by

$$E_{\mathrm{B}} = \frac{L^3 m}{4bt^3} \tag{10}$$

where m is the slope of the force-deflection curve. When modeling different configurations of MMSSs, the geometric parameters in Eq. (10) remain the same.

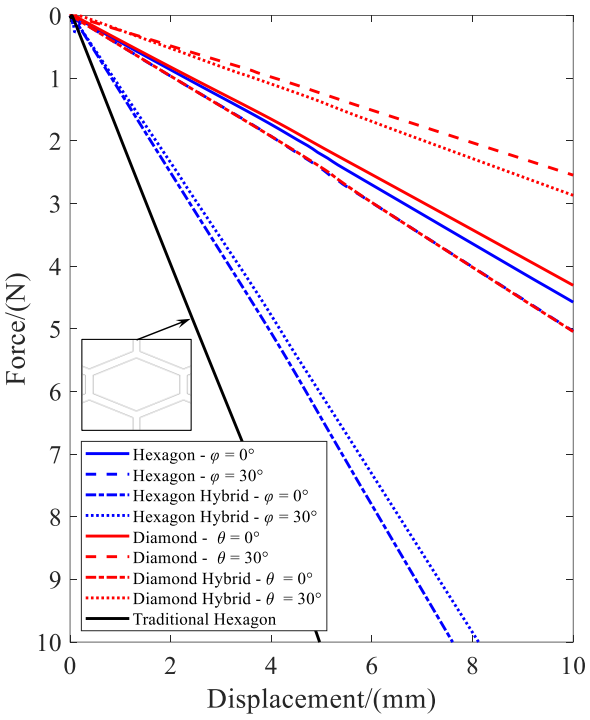

(a)

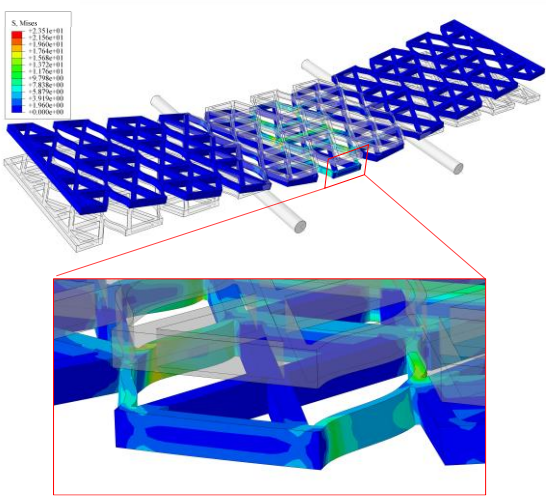

(b)

Figure 18. Results of the standard three-point bending test: (a) Force-deflection curve (b) FEM results.

Therefore, the bending stiffness of the structure is solely dependent on the slope of the load-deflection curve. Under the same array form, MMSSs composed of hexagonal units have greater bending stiffness compared to those composed of diamond-shaped units. Within the diamond-shaped base units, the linear array lattice metamaterial with "U"-shaped support structures exhibits greater bending stiffness than that with "Y"-shaped support structures. Utilizing hybrid arrays can enhance the bending stiffness of the structure without increasing the mass, as it only involves rearranging the unit cells.

For hexagonal units, the linear array MMSSs with "H"-shaped support structures has greater bending stiffness than that with "X"-shaped support structures, which is the opposite conclusion from the MMSSs composed of diamond-shaped units. Employing hybrid arrays significantly improves the structure's bending stiffness, with the enhancement being much greater than that of diamond-shaped units. However, the mass will inevitably increase to maintain structural integrity.

As shown in Fig. 18(a), the use of BPCBs reduces the bending stiffness of MMSSs compared to traditional hexagon honeycomb structures. This is due to the thinner BPCB reducing the driving force and the curved beam configuration leading to a decrease in local torsional stiffness compared to a straight beam. Therefore, the bending stiffness of traditional hexagonal honeycombs is greater than that of all multi-stable lattice metamaterials. Figure 18(b) shows the finite element simulation results for hexagonal hybrid arrays. The enlarged local view reveals that the structure mainly undergoes local torsional deformation of the BPCBs under bending loads. Future work can optimize the cross-section or curve of the BPCBs to significantly enhance the torsional stiffness while maintaining low bending stiffness [28]. This approach can improve the bending stiffness of the structure while reducing the driving force requirements for the actuators for morphing system.

4.4. The influences of key structural parameters

This section investigates the influences of key structural parameters of the structure on its bending stiffness. To fully account for the influence of structural geometric parameter on structural mass, the specific bending modulus E_{B}^{*} is calculated by computing the relative density ρ^{*} and bending modulus of the MMSS. Since the materials used for the honeycomb are homogeneous here and the structure is two-dimensional, so the relative density equals the ratio of the actual area occupied by the honeycomb A_{c} to the rectangular area A_{s} of the honeycomb. The actual area occupied by the honeycomb is directly derived from the modeling software Catia. The expression for the specific bending modulus is given by

$$E_{\mathrm{B}}^{*}=\frac{E_{\mathrm{B}}}{\rho^{*}}=\frac{E_{\mathrm{B}}}{A_{\mathrm{c}}/A_{\mathrm{s}}} \tag{11}$$

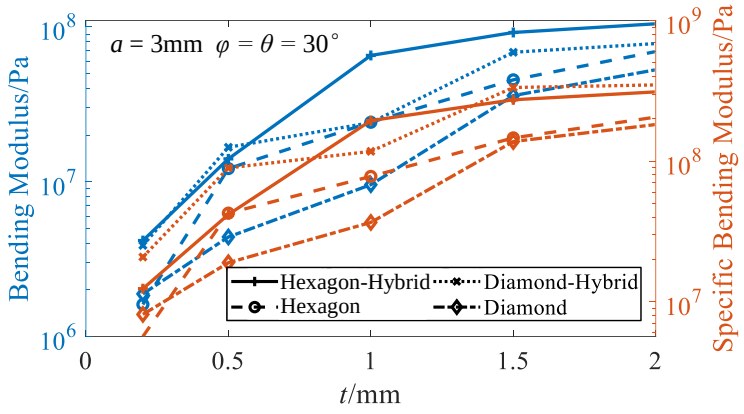

(a)

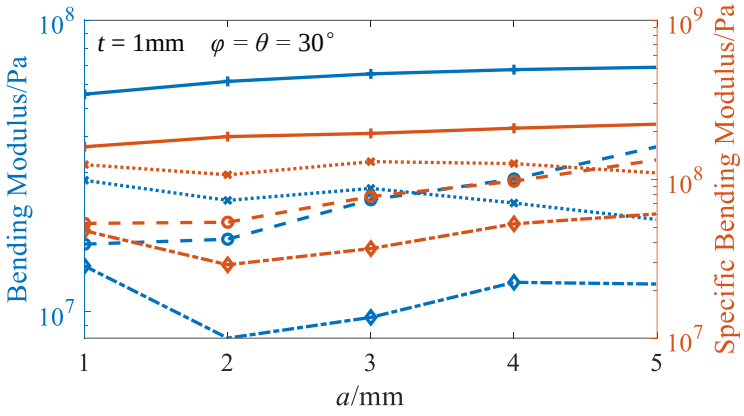

(b)

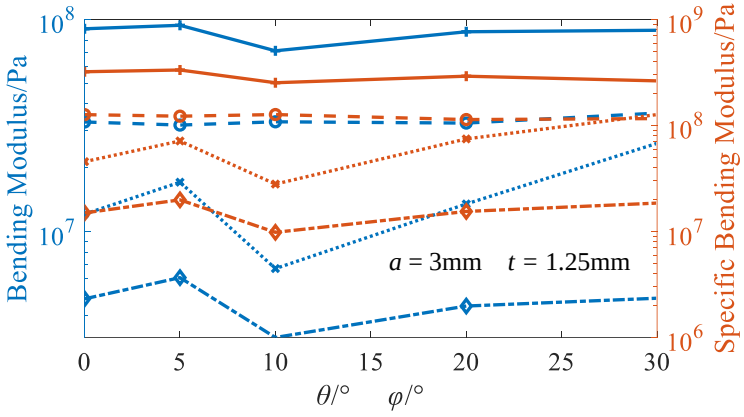

(c)

Figure 19. The influence of key structural parameters on bending stiffness: (a) Different curved beam thicknesses (b) Different curved beam heights (c) Different inclination angle.

The influence of the thickness t and height $2a$ of the BPCB on the bending stiffness and specific bending stiffness of the structure is shown in Figs. 19(a) and 19(b). The effect of the tilt angle of the supporting structure on the bending stiffness and specific bending stiffness of the structure is shown in Fig. 19(c). The left vertical axis corresponding to the blue line represents

the bending modulus calculated by Eq. (10) and the right vertical axis corresponding to the orange line represents the specific bending modulus calculated by Eq. (11). It can be observed that the trend of changes in bending modulus and specific bending modulus is consistent.

The thickness of the curved beam has the most influence on the bending modulus of the structure. Once the thickness of the curved beam increases, the bending modulus of all MMSS increases significantly, although the rate of increase slows down. The height of the BPCB has little influence on the bending modulus of the structure. In the series of hexagonal units, the bending modulus slightly increases with the height of the curved beam. In the series of diamond-shaped units, a fluctuating trend is observed. The inclination angle of the supporting structure also has a minor impact on the bending modulus of the structure, generally showing a fluctuating trend. It can be seen that both the diamond-shaped units with "U" shaped support structure and hexagonal units with "H" shaped support structure has an inclination angle of 0°. The main purpose to analyze the inclination angle of the supporting structure is to highlight certain advantages in the subsequent processing of morphing skins and in avoiding wrinkles in a flexible surface layer. For the support structure with an inclination angle of 0°, the flat boundary condition of the flexible surface layer can to some extent prevent the bulge effect caused by stress concentration [54,55].

After considering the mass changes caused by the array form, the specific bending modulus still shows that the MMSS with a hybrid array is much better than that of the linear array. This fully demonstrates that such novel array form significantly enhances the bending stiffness of the MMSS while maintaining the structural mass.

5. Conclusions

This paper introduces a design scheme for a MMSS and examines the steady-state switching, mechanical response, and the impact of critical structural parameters on the in-plane and out-of-plane mechanical properties using theoretical, numerical and experimental methods.

A theoretical model for the in-plane large deformation of the MMSS was developed based on the theory of large deformation beams and potential energy landscape approaches. This model shows good agreement with the FEM and experimental results, providing a rapid analysis method for mechanical characteristics during the initial design phase. Different stable states can be switched through appropriate structural design without required external force maintenance compared to traditional metamaterial structures.

A numerical model for the out-of-plane deformation of the MMSS was established by Abaqus. Standard three-point bending tests show that BPCB-based honeycomb structures have significantly lower bending stiffness compared to traditional honeycomb structures. The thickness of the BPCB having the most significant impact on bending stiffness, and the bending stiffness of MMSSs based on hexagonal units is generally more critical than those based on diamond-shaped units.

MMSSs in the hybrid array form proposed in this study enhances bending stiffness by more than twofold relative to MMSSs in the conventional linear array, approaching the out-of-plane bending stiffness of traditional honeycomb structures.

This design and analysis method can be extended to designing multi-stable modules based on different bi-stable units and analyzing of deformation requirements in multiple dimensions.

Acknowledgments

This project has received funding from National Natural Science Foundation of China (Grant No. 92271104, 12102017, 52305262) and Beijing Natural Science Foundation (Grant No. 1232014).

References

1 Barbarino, S., Bilgen, O., Ajaj, R. M., Friswell, M. I., and Inman, D. J. "A Review of Morphing Aircraft," *Journal of Intelligent Material Systems and Structures*, Vol. 22, No. 9, 2011, pp. 823-877.
doi: 10.1177/1045389x11414084

2 Reich, G., and Sanders, B. "Introduction to Morphing Aircraft Research," *Journal of Aircraft*, Vol. 44, No. 4, 2007, pp. 1059-1059.
doi: 10.2514/1.28287

3 Stanewsky, E. "Aerodynamic Benefits of Adaptive Wing Technology," *Aerospace Science and Technology*, Vol. 4, No. 7, 2000, pp. 439-452.
doi: 10.1016/s1270-9638(00)01069-5

4 Molinari, G., Arrieta, A. F., Guillaume, M., and Ermanni, P. "Aerostructural Performance of Distributed Compliance Morphing Wings: Wind Tunnel and Flight Testing," *AIAA Journal*, Vol. 54, No. 12, 2016, pp. 3859-3871.
doi: 10.2514/1.J055073

5 Weisshaar, T. A. "Morphing Aircraft Systems: Historical Perspectives and Future Challenges," *Journal of Aircraft*, Vol. 50, No. 2, 2013, pp. 337-353.
doi: 10.2514/1.C031456

6 Thill, C., Etches, J., Bond, I., Potter, K., and Weaver, P. "Morphing Skins," *The Aeronautical Journal*, Vol. 112, No. 1129, 2008, pp. 117-139.
doi: 10.1017/S0001924000002062

7 Olympio, K. R., and Gandhi, F. "Zero Poisson's Ratio Cellular Honeycombs for Flex Skins Undergoing One-Dimensional Morphing," *Journal of Intelligent Material Systems and Structures*, Vol. 21, No. 17, 2009, pp. 1737-1753. doi: 10.1177/1045389x09355664

8 Gao, J., Cao, X., Xiao, M., Yang, Z., Zhou, X., Li, Y., Gao, L., Yan, W., Rabczuk, T., and Mai, Y.-W. "Rational designs of mechanical metamaterials: Formulations, architectures, tessellations and prospects," *Materials Science and Engineering: R: Reports*, Vol. 156, 2023, p. 100755. doi: 10.1016/j.mser.2023.100755

9 Bertoldi, K., Vitelli, V., Christensen, J., and van Hecke, M. "Flexible Mechanical Metamaterials," *Nature Reviews Materials*, Vol. 2, No. 11, 2017, p. 17066. doi: 10.1038/natrevmats.2017.66

10 Vasista, S., Tong, L., and Wong, K. C. "Realization of Morphing Wings: A Multidisciplinary Challenge," *Journal of Aircraft*, Vol. 49, No. 1, 2012, pp. 11-28. doi: 10.2514/1.C031060

11 Zheng, J., Li, R., Zhong, W., and Li, Y. "A Bio-OCLC Structure Equating to a Movable Unit of a Lattice Cellular Core for Hybrid In-Plane Morphing Applications," *Composite Structures*, Vol. 235, 2020, p. 111762. doi: 10.1016/j.compstruct.2019.111762

12 Li, X., Peng, W., Wu, W., Xiong, J., and Lu, Y. "Auxetic Mechanical Metamaterials: From Soft to Stiff," *International Journal of Extreme Manufacturing*, Vol. 5, No. 4, 2023, p. 042003. doi: 10.1088/2631-7990/ace668

13 Olympio, K. R., and Gandhi, F. "Flexible Skins for Morphing Aircraft Using Cellular Honeycomb Cores," *Journal of Intelligent Material Systems and Structures*. Vol. 21, No. 17, 2009, pp. 1719-1735. doi: 10.1177/1045389x09350331

14 Bubert, E. A., Woods, B. K. S., Lee, K., Kothera, C. S., and Wereley, N. M. "Design and Fabrication of a Passive 1D Morphing Aircraft Skin," *Journal of Intelligent Material Systems and Structures*. Vol. 21, No. 17, 2010, pp. 1699-1717. doi: 10.1177/1045389x10378777

15 Dayyani, I., Khodaparast, H. H., Woods, B. K. S., and Friswell, M. I. "The Design of a Coated Composite Corrugated Skin for the Camber Morphing Airfoil," *Journal of Intelligent Material Systems and Structures*. Vol. 26, No. 13, 2014, pp. 1592-1608. doi: 10.1177/1045389x14544151

16 Alderson, A., Alderson, K. L., Chirima, G., Ravirala, N., and Zied, K. M. "The In-Plane Linear Elastic Constants and Out-Of-Plane Bending of 3-Coordinated Ligament and Cylinder-ligament Honeycombs," *Composites Science and Technology*. Vol. 70, No. 7, 2010, pp. 1034-1041. doi: 10.1016/j.compscitech.2009.07.010

17 Li, X., Li, Z., Guo, Z., Mo, Z., and Li, J. "A Novel Star-Shaped Honeycomb with Enhanced Energy Absorption," *Composite Structures*. Vol. 309, 2023, Paper 116716. doi: 10.1016/j.compstruct.2023.116716

18 Liu, W., Li, H., Zhang, J., Gong, X., Wang, Y., and Ge, X. "Tensile and Shear Properties of Star-Shaped Cellular Lattice Structure," *Mechanics of Advanced Materials and Structures*, Vol. 28, No. 24, 2021, pp. 2605-2617. doi: doi:10.1080/15376494.2020.1747669

19 Huang, J., Zhang, Q., Scarpa, F., Liu, Y., and Leng, J. "In-Plane Elasticity of a Novel Auxetic Honeycomb Design," *Composites Part B: Engineering*, Vol. 110, 2017, pp. 72-82. doi: 10.1016/j.compositesb.2016.11.011

20 Chen, J., Shen, X., and Li, J. "Zero Poisson's Ratio Flexible Skin for Potential Two-Dimensional Wing Morphing," *Aerospace Science and Technology*, Vol. 45, 2015, pp. 228-241.

doi: 10.1016/j.ast.2015.05.011

21 Jha, A., and Dayyani, I. "Shape Optimisation and Buckling Analysis of Large Strain Zero Poisson's Ratio Fish-Cells Metamaterial for Morphing Structures," *Composite Structures*, Vol. 268, 2021, p. 113995.
doi: 10.1016/j.compstruct.2021.113995

22 Wan, G., Avis, S. J., Wang, Z., Wang, X., Kusumaatmaja, H., and Zhang, T. "Finding Transition State and Minimum Energy Path of Bistable Elastic Continua Through Energy Landscape Explorations," *Journal of the Mechanics and Physics of Solids*, Vol. 183, 2024, p. 105503.
doi: 10.1016/j.jmps.2023.105503

23 Zhang J., Zhang, C., Hao, L., Nie, R. and Qiu, J., Exploiting the Instability of Smart Structure for Reconfiguring. *Applied Physics Letters*, Vol.111, No. 6, 2017, p. 064102. doi: 10.1063/1.4986795

24 Xu, R., Chen, C., Sun, J., He, Y., Li, X., Lu, M.-H., and Chen, Y. "The Design, Manufacture and Application of Multistable Mechanical Metamaterials-a State of the Art Review," *International Journal of Extreme Manufacturing*, Vol. 5, No. 4, 2023, p. 042013.
doi: 10.1088/2631-7990/acf96a

25 Zhang, L., Pan, F., Ma, Y., Yang, K., Guo, S., and Chen, Y. "Bistable Reconfigurable Origami Metamaterials with High Load-Bearing and Low State-Switching Forces," *Extreme Mechanics Letters*, Vol. 63, 2023, p. 102064.
doi: 10.1016/j.eml.2023.102064

26 Findeisen, C., Hohe, J., Kadic, M., and Gumbsch, P. "Characteristics of Mechanical Metamaterials Based on Buckling Elements," *Journal of the Mechanics and Physics of Solids*, Vol. 102, 2017, pp. 151-164.
doi: 10.1016/j.jmps.2017.02.011

27 Liu, M., Domino, L., Dupont de Dinechin, I., Taffetani, M., and Vella, D. "Snap-Induced Morphing: From a Single Bistable Shell to the Origin of Shape Bifurcation in Interacting Shells," *Journal of the Mechanics and Physics of Solids*, Vol. 170, 2023, p. 105116.
doi: 10.1016/j.jmps.2022.105116

28 Chen, G., Wu, H., Li, B., and Wang, M. Y. "Fully Compliant Bistable Mechanisms with Enhanced Pitch Stiffness," *Mechanical Systems and Signal Processing*, Vol. 161, 2021, p. 107926.
doi: 10.1016/j.ymssp.2021.107926

29 Wheatcroft, E. D., Shen, J., Groh, R. M. J., Pirrera, A., and Schenk, M. "Structural Function from Sequential, Interacting Elastic Instabilities," *Proceedings of the Royal Society A: Mathematical, Physical and Engineering Sciences*, Vol. 479, No. 2272, 2023, p. 220861.
doi: 10.1098/rspa.2022.0861

30 Liu, Y., Zhang, J., Pan, D., Wu, Z., and Wang, Q. "Resonant Actuation Based on Dynamic Characteristics of Bistable Laminates," *Machines*, Vol. 11, No. 3, 2023, p. 318.
doi: 10.3390/machines11030318

31 Schenk, M., and Guest, S. D. "On Zero Stiffness," *Proceedings of the Institution of Mechanical Engineers, Part C: Journal of Mechanical Engineering Science*, Vol. 228, No. 10, 2013, pp. 1701-1714.
doi: 10.1177/0954406213511903

32 Li, Y., Pan, F., Lin, X., Yang, K., Ren, Y., Yang, W., and Chen, Y. "Multistable Origami Honeycomb," *International Journal of Mechanical Sciences*, Vol. 243, 2023, p. 108044.
doi: 10.1016/j.ijmecsci.2022.108044

33 Pirrera, A., Lachenal, X., Daynes, S., Weaver, P. M., and Chenchiah, I. V. "Multi-stable Cylindrical Lattices," *Journal of the Mechanics and Physics of Solids*, Vol. 61, No. 11, 2013, pp. 2087-2107.
doi: 10.1016/j.jmps.2013.07.008

34 Xi, K., Chai, S., Ma, J., and Chen, Y. "Multi-Stability of the Extensible Origami Structures," *Advanced Science*, Vol.

10, No. 29, 2023, p. e2303454.
doi: 10.1002/advs.202303454

35 Fang, H., Li, S., Ji, H., and Wang, K. W. "Dynamics of a Bistable Miura-Origami Structure," *Physical Review E*, Vol. 95, No. 5-1, 2017, p. 052211.
doi: 10.1103/PhysRevE.95.052211

36 Abbasi, A., Sano, T. G., Yan, D., and Reis, P. M. "Snap Buckling of Bistable Beams Under Combined Mechanical and Magnetic Loading," *Philosophical Transactions of the Royal Society A-Mathematical Physical and Engineering Sciences*, Vol. 381, No. 2244, 2023, p. 20220029.
doi: 10.1098/rsta.2022.0029

37 Restrepo, D., Mankame, N. D., and Zavattieri, P. D. "Programmable Materials Based on Periodic Cellular Solids. Part I: Experiments," *International Journal of Solids and Structures*, Vol. 100-101, 2016, pp. 485-504.
doi: 10.1016/j.ijsolstr.2016.09.021

38 Restrepo, D., Mankame, N. D., and Zavattieri, P. D. "Phase Transforming Cellular Materials," *Extreme Mechanics Letters*, Vol. 4, 2015, pp. 52-60.
doi: 10.1016/j.eml.2015.08.001

39 Shi, J., Mofatteh, H., Mirabolghasemi, A., Desharnais, G., and Akbarzadeh, A. "Programmable Multistable Perforated Shellular," *Advanced Materials*, Vol. 33, No. 42, 2021.
doi: 10.1002/adma.202102423

40 Chen, T., Pauly, M., and Reis, P. M. "A Reprogrammable Mechanical Metamaterial with Stable Memory," *Nature*, Vol. 589, No. 7842, 2021, pp. 386-390.
doi: 10.1038/s41586-020-03123-5

41 Mei, T., Meng, Z., Zhao, K., and Chen, C. Q. "A Mechanical Metamaterial with Reprogrammable Logical Functions," *Nature Communication*, Vol. 12, No. 1, 2021, p. 7234.
doi: 10.1038/s41467-021-27608-7

42 Boston, D. M., Phillips, F. R., Henry, T. C., and Arrieta, A. F. "Spanwise Wing Morphing Using Multistable Cellular Metastructures," *Extreme Mechanics Letters*, Vol. 53, 2022, p. 101706.
doi: 10.1016/j.eml.2022.101706

43 Boston, D. M., and Arrieta, A. F. "Homogenization Model for Multistable Honeycomb Metastructures Exhibiting Beam-like Behavior," *AIAA SCITECH 2023 Forum*, AIAA 2023-1394, 2023.
doi: 10.2514/6.2023-1394

44 Udani, J. P., and Arrieta, A. F. "Taming Geometric Frustration by Leveraging Structural Elasticity," *Materials & Design*, Vol. 221, 2022.
doi: 10.1016/j.matdes.2022.110809

45 Udani, J. P., and Arrieta, A. F. "Programmable Mechanical Metastructures from Locally Bistable Domes," *Extreme Mechanics Letters*, Vol. 42, 2021.
doi: 10.1016/j.eml.2020.101081

46 Faber, J. A., Udani, J. P., Riley, K. S., Studart, A. R., and Arrieta, A. F. "Dome-Patterned Metamaterial Sheets," *Advanced Science*, Vol. 7, No. 22, 2020.
doi: 10.1002/advs.202001955

47 Shaw, A. D., Zhang, J., Wang, C., Woods, B. K. S., and Friswell, M. I. "System-Level Optimization of Passive Energy Balancing," *AIAA Journal*, Vol. 60, No. 9, 2022, pp. 5570-5580.
doi: 10.2514/1.J061959

48 Zhang, J., Shaw, A. D., Amoozgar, M., Friswell, M. I., and Woods, B. K. S. "Bidirectional Torsional Negative Stiffness Mechanism for Energy Balancing Systems," *Mechanism and Machine Theory*, Vol. 131, 2019, pp. 261-277.

doi: 10.1016/j.mechmachtheory.2018.10.003

49 Qiu, J., Lang, J. H., and Slocum, A. H. "A Curved-Beam Bistable Mechanism," *Journal of Microelectromechanical Systems*, Vol. 13, No. 2, 2004, pp. 137-146.
doi: 10.1109/jmems.2004.825308

50 Hussein, H., Le Moal, P., Bourbon, G., Haddab, Y., and Lutz, P. "Modeling and Stress Analysis of a Pre-Shaped Curved Beam: Influence of High Modes of Buckling," *International Journal of Applied Mechanics*, Vol. 07, No. 04, 2015, p. 1550055.
doi: 10.1142/s1758825115500556

51 Oh, Y. S., and Kota, S. "Synthesis of Multistable Equilibrium Compliant Mechanisms Using Combinations of Bistable Mechanisms," *Journal of Mechanical Design*, Vol. 131, No. 2, 2009, p. 021002.
doi: 10.1115/1.3013316

52 Tan, X., Wang, B., Wang, L., Zhu, S., Chen, S., Yao, K., and Xu, P. "Effect of Beam Configuration on its Multistable and Negative Stiffness Properties," *Composite Structures*, Vol. 286, 2022, p. 115308.
doi: 10.1016/j.compstruct.2022.115308

53 Dal, H., Açıkgöz, K., and Badienia, Y. "On the Performance of Isotropic Hyperelastic Constitutive Models for Rubber-Like Materials: A State of the Art Review," *Applied Mechanics Reviews*, Vol. 73, No. 2, 2021.
doi: 10.1115/1.4050978

54 Ahmad, D., Ajaj, R. M., and Amoozgar, M. "Elastomer-Based Skins for Morphing Aircraft Applications: Effect of Biaxial Strain Rates and Prestretch," *Polymer Testing*, Vol. 113, 2022, p. 107655.
doi: 10.1016/j.polymertesting.2022.107655

55 You, H., Kim, S., and Yun, G. J. "Design Criteria for Variable Camber Compliant Wing Aircraft Morphing Wing Skin," *AIAA Journal*, Vol. 58, No. 2, 2020, pp. 867-878.
doi: 10.2514/1.J058002